



Efficient photocatalytic H₂ evolution using NiS/ZnIn₂S₄ heterostructures with enhanced charge separation and interfacial charge transfer

Aihua Yan^{a,b}, Xiaowei Shi^b, Fei Huang^a, Mamoru Fujitsuka^b, Tetsuro Majima^{b,*}

^a Low Carbon Energy Institute, China University of Mining and Technology, Xuzhou 221008, China

^b The Institute of Scientific and Industrial Research (SANKEN), Osaka University, Mihogaoka 8-1, Ibaraki, Osaka, 567-0047, Japan



ARTICLE INFO

Keywords:
NiS/ZnIn₂S₄ heterostructure
Hydrogen evolution
Band alignment
Interfacial charge transfer
Charge separation efficiency

ABSTRACT

The effect of multidimensional heterostructures on charge transfer and charge separation is intriguing in photocatalytic applications. Herein, NiS/ZnIn₂S₄ heterostructures with tailororable composition, tunable light absorption, and controllable band gap were successfully prepared by a two-step method to show uniform NiS nanoparticles with an average size of 10 nm loaded homogeneously on porous ZnIn₂S₄ nanosheets. Consequently, NiS/ZnIn₂S₄ heterostructures have markedly enhanced light absorption and efficient photocatalytic efficiency, reaching the hydrogen evolution rate of 5.0 $\mu\text{mol h}^{-1}$ under the light irradiation at 420 nm, to be approximately three times higher than that of pure ZnIn₂S₄. The enhanced photocatalytic efficiency results from faster charge transfer and more efficient photogenerated electron-hole separation under beneficial band alignment. The results shed light on how the photocatalytic reaction occurs at the interface between NiS and ZnIn₂S₄, and can open a new avenue for synthesizing efficient photocatalysts.

1. Introduction

Two-dimensional (2D) metal chalcogenides with atomically layered structure, due to their special optoelectronic and photochemical properties, are an kind of ideal low-dimensional system for photocatalytic applications, as well as an elemental building block for designed assembly [1–3]. Among the reported 2D chalcogenides, ZnIn₂S₄ has recently attracted considerable interests because of the low cost, high photostability, and low toxicity. However, ZnIn₂S₄ exhibits no admirable efficiency for light utilization because of the relatively wide band gap (2.4–2.8 eV) and slow charge transfer [4–6].

As an important strategy, unexceptionable functionalities can be rationally tailored through precise molecular-scale control and coordination of artificial 2D heterostructures [7–9]. Usually, intriguing interfacial effects and unique physicochemical properties have been gradually uncovered in 2D hetero-layered materials due to their large surface-to-volume ratios to cause strong adsorption, confined thickness at an atomic scale to cause shorter charge transport, wide spectrum absorption to cause charge separation with higher efficiency, and moderate built-in electric field at the interface to suppress the electron-hole recombination [10–13]. Although various heterostructures have been developed for the efficient ZnIn₂S₄ photocatalysis, lattice mismatching for PVD/CVD methods and weak dispersibility for wet-chemical methods hinder composition customization of heterostructures

[14,15]. Therefore, it is still a great challenge for aforementioned issues to realize hetero-layered ZnIn₂S₄ nanosheets.

Herein, a two-step method was used to synthesize NiS nanoparticles (NS) loaded on porous ZnIn₂S₄ nanosheets (ZIS) heterostructures (NS/ZIS), forming a kind of intimate-contact heterostructures between NS and ZIS (Fig. 1a). Achieving this goal should initially prepare porous ZIS nanosheets through a hydrothermal method. Then, by virtue of ZIS configuration with large surface area, NS nanoparticles were loaded on ZIS platform during the photodeposition process. The detailed procedure is described in Supplementary Information (Experimental Section). 5, 10, 25, 50, 100, and 500 μL Ni²⁺ solutions resulted in NS loading amounts of 0.11, 0.22, 0.55, 1.1, 2.2, and 11 wt% in NS/ZIS-x where x denotes the volume of Ni²⁺ solutions in μL , respectively (Table 1S). The band-gap excitation, transfer, and recombination processes were thoroughly investigated by monitoring the transient absorption spectral changes and photoelectrochemical properties.

2. Results and discussion

The structures of as-prepared ZIS and NS/ZIS-x were characterized by field emission scanning electron microscopy (FESEM) and transmission electron microscopy (TEM). The size distribution of hierarchical ZIS is in the range of 5–15 μm with curly structure (Fig. 1b). TEM and AFM images further confirm the hierarchical architecture

* Corresponding author.

E-mail address: majima@sanken.osaka-u.ac.jp (T. Majima).

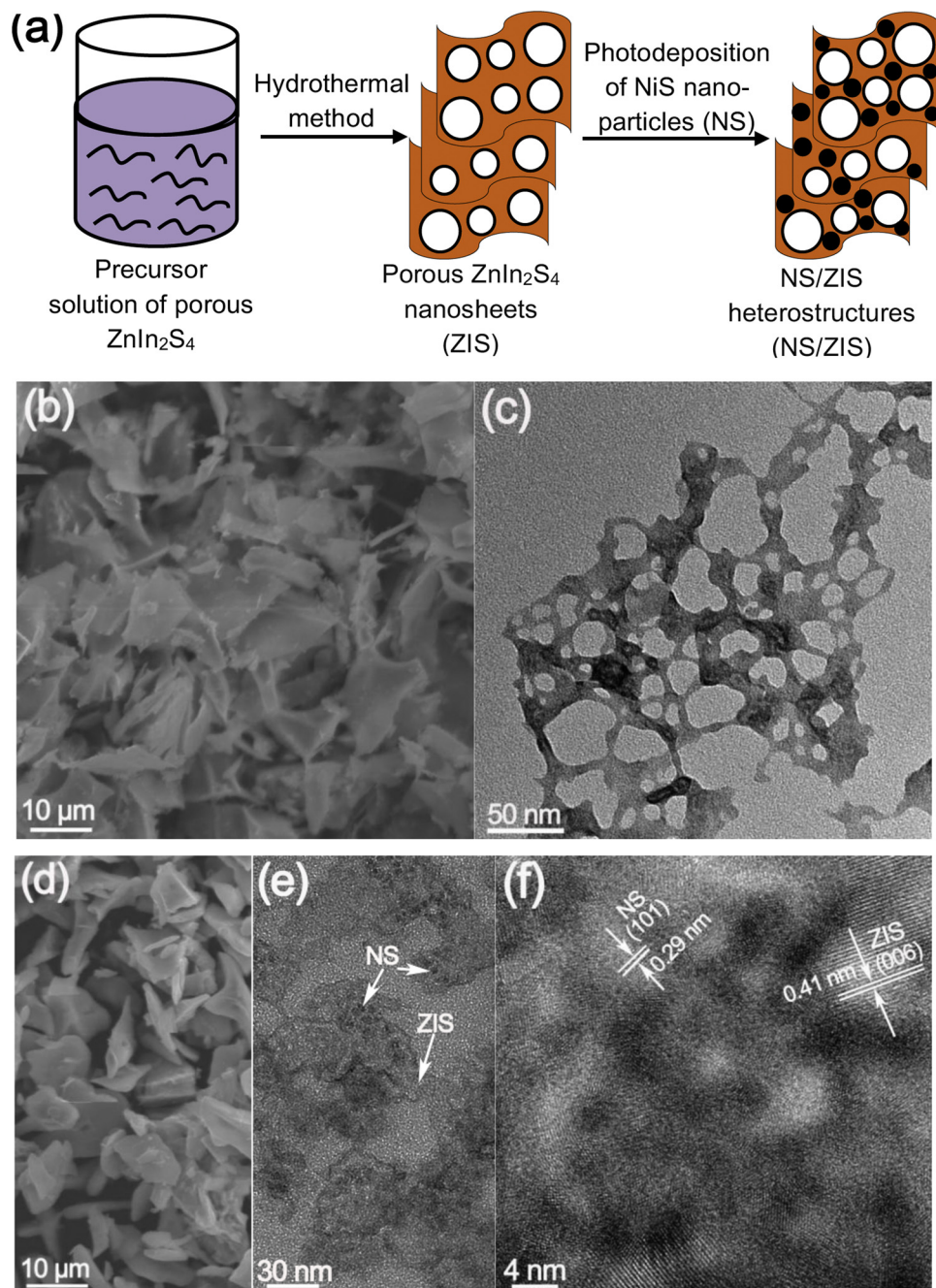


Fig. 1. Synthesis of NS/ZIS-x (a). FESEM and TEM images of pure ZIS (b, c) and NS/ZIS-10 (d, e, and f).

composed of ZIS with pore diameters of 20–80 nm and a thickness of 8–9 nm (Fig. 1c, Supporting information Figure S1). The morphology, thickness, and pore size were modulated by the amounts of sodium citrate (Supporting information Figure S2). NS/ZIS-x exhibits similar morphology and structure to pure ZIS (Fig. 1d). As evidenced by TEM image, it is distinct to observe the successful hybridization of ZIS with NS (Fig. 1e). NS nanoparticles with the average size of 8–10 nm are uniformly distributed on ZIS. HRTEM image further demonstrates that both ZIS and NS are highly crystallized. The well-resolved characteristic lattice fringes of 0.41 and 0.29 nm are in agreement with the (006) plane of 2H-ZIS and (101) plane of NS, respectively (Fig. 1f), further confirming the successful hybridization of ZIS with NS.

The crystal structures of as-synthesized ZIS and NS/ZIS-x were identified by X-ray diffraction (XRD). As shown in Fig. 2a, all samples have the characteristic peaks assigned to (006), (102), and (110) crystal

planes of hexagonal ZIS (JCPDS No. 72-0773, $a = b = 3.85$, $c = 24.68$). No additional impurity such as ZnS and In_2S_3 is observed in pure ZIS. Moreover, no diffraction peak corresponding to NS is observed in NS/ZIS-x, indicating that low NS loading has no influence on the structure of ZIS (Supporting information Figure S3). However, the existence of NS is found by the corresponding EDX spectrum (Fig. 2b). The corresponding EDX mapping images unequivocally confirm the homogeneous distribution of Zn, In, and S in NS/ZIS-10 (Fig. 2c–e). Specially, Ni element mainly distributes at the edge of nanopores, further confirming the possible formation of NS/ZIS-10 (Fig. 2f).

XPS analyses were carried out to further study the chemical states of pure ZIS and NS/ZIS-x. As shown in Fig. 3a, all elements, including Zn, In, S, and C, are detected. It should be noted that C element originates from the conducting resin. Characteristic binding energy of 1022.8 and 1045.8 eV for $\text{Zn } 2\text{p}_{3/2}$ and $\text{Zn } 2\text{p}_{1/2}$, 444.8 and 445.8 eV for $\text{In } 3\text{d}_{5/2}$

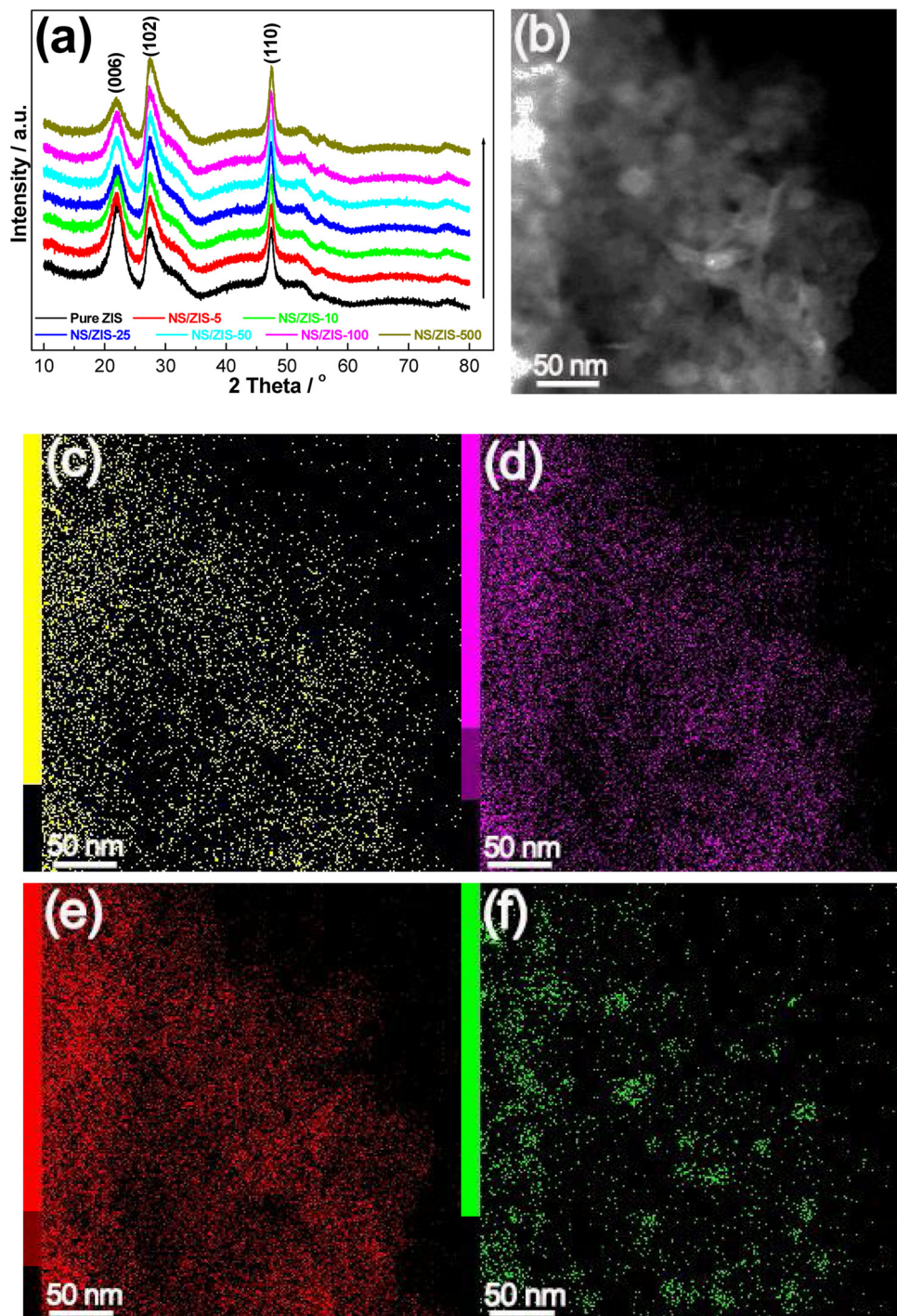


Fig. 2. XRD patterns of pure ZIS and NS/ZIS-x (a). SEM image of NS/ZIS-10 (b). Elemental mappings of Zn (c), In (d), S (e), and Ni (f) in NS/ZIS-10.

and In 3d_{3/2}, respectively, are observed in NS/ZIS-x (Fig. 3b and c) [16,17]. Besides, the peaks at 162.6 and 163.8 eV correspond to S 2p_{3/2} and S 2p_{1/2}, respectively (Fig. 3d) [12,18]. The Ni 2p spectrum in Fig. 3e clearly demonstrates three peaks at 858.4, 854.7, and 852.4 eV to be assigned to Ni 2p_{3/2}, the main peak and satellite peak of Ni 2p_{1/2} in NS/ZIS-x, respectively [19,20]. That is, the samples include NS phase. Compared to those observed in pure ZIS, the peaks of S 2p and In 3d in NS/ZIS-x slightly shift toward lower binding energy (Fig. 3f, Supporting information Figure S4). The shift of the binding energy suggests a strong electronic interaction or the formation of heterostructure between NS and ZIS in NS/ZIS-x (Fig. 3f).

Steady-state UV-vis diffuse reflection spectra (DRS) were measured

to study optical properties of as-prepared samples. As shown in Fig. 4a, pure ZIS has the absorption edge at 599 nm but no absorption in the range of 600–1100 nm. After loading NS on ZIS, the absorption peak obviously becomes stronger and broader in UV-vis region. The absorption edges of NS/ZIS-x shift from 599 nm to 750 nm due to the absorption of the incorporated NS (Table 1). Furthermore, the red shifts of NS/ZIS-x are mainly controlled by the loaded NS with a high refractive index, implying the efficient utilization of solar light and higher charge separation. The Kubelka-Munk equation is written in Eq.(1) [21]:

$$(ah\nu)^n = A(h\nu - E_g) \quad (1)$$

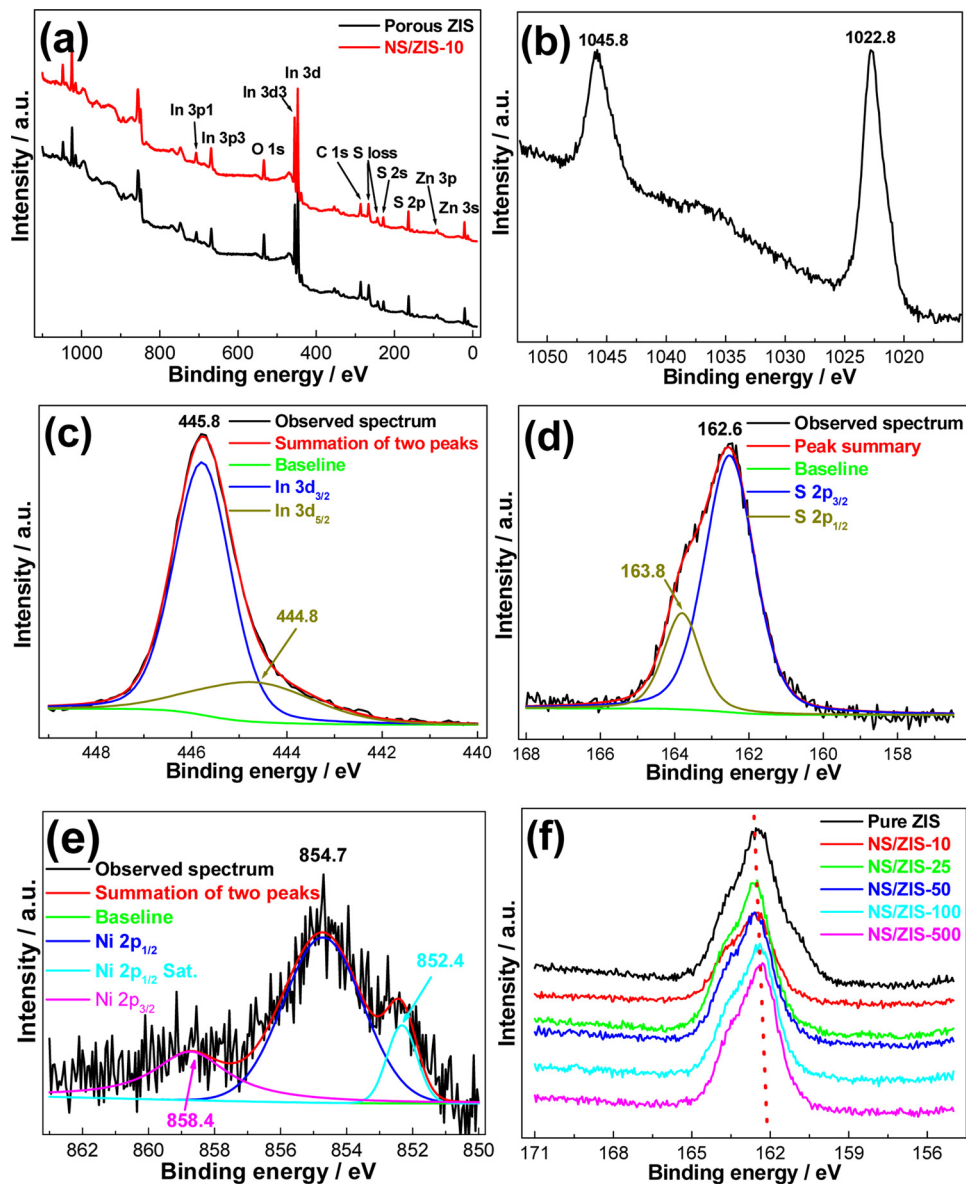


Fig. 3. Wide-scan XPS spectra of pure ZIS and NS/ZIS-10 (a), narrow-scan XPS spectra of Zn 2p (b), In 3d (c), S 2p (d), Ni 2p (e), and S 2p (f) in NS and NS/ZIS-x.

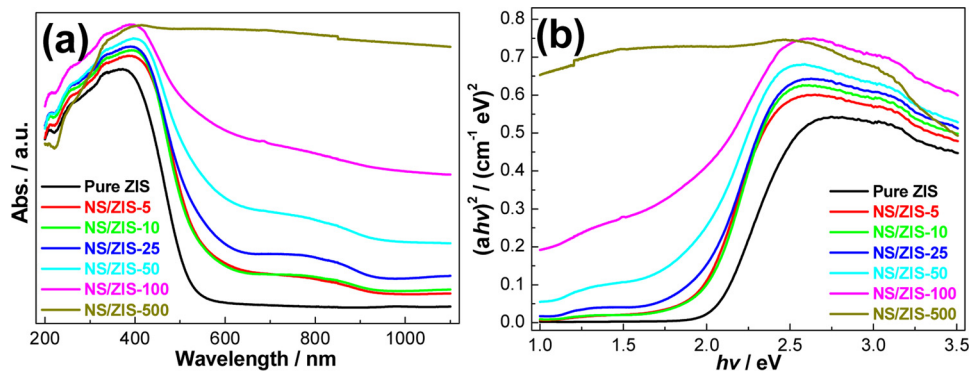


Fig. 4. UV-vis absorption spectra (a) and relations of $(ahv)^{1/2}$ vs. $h\nu$ curves (b) for ZIS and NS/ZIS-x.

where α , $h\nu$, n , A , and E_g are absorption coefficient, photon energy, parameter connected to the distribution of density of states, Tauc's constant, and band gap, respectively. It can be seen that NS/ZIS-x has narrower band gap, as shown in Fig. 4b. Usually, the narrower band gap exerts favorable effects on light absorption and photocatalytic

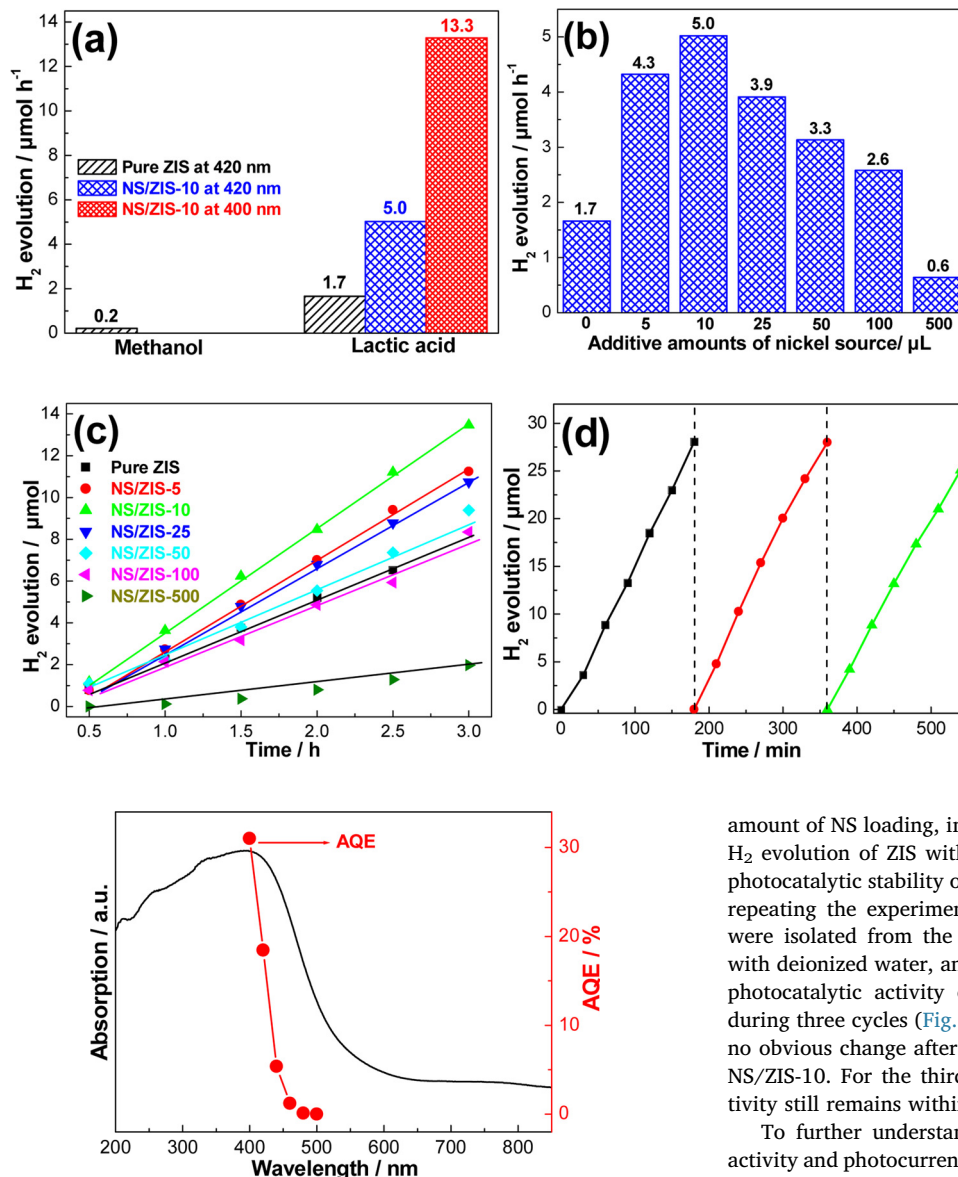
performance [22,23].

Photocatalytic hydrogen (H_2) evolution experiments were carried out over as-prepared ZIS and NS/ZIS-x in the presence of methanol and lactic acid as sacrificial agents under the irradiation at 400 or 420 nm for 3 h. Notably, methanol is not a suitable sacrificial agent for ZIS and

Table 1

Absorption edges and calculated band gaps for pure ZIS and NS/ZIS-x.

Samples	ZIS	NS/ZIS-5	NS/ZIS-10	NS/ZIS-25	NS/ZIS-50	NS/ZIS-100
Absorption edges (nm)	599	629	632	635	677	750
Band gaps (eV)	2.07	1.97	1.96	1.95	1.83	1.65

**Fig. 6.** UV-vis spectrum and AQE of NS/ZIS-10.

NS/ZIS-x, compared to lactic acid (Fig. 5a). Then, we measured the average rates of H_2 evolution using pure ZIS and NS/ZIS as the photocatalysts in the presence of lactic acid without any additive Pt co-catalyst under the irradiation at 420 nm. Clearly, a quasi-normal distribution for H_2 evolution was obtained with the highest rate of $5.0 \mu\text{mol h}^{-1}$ for NS/ZIS-10 (Fig. 5b). This efficiency is approximately three times of that for pure ZIS with a rate of $1.7 \mu\text{mol h}^{-1}$. Subsequently, it decreases with further increasing NS loading, due to the “light-shielding effect” [24,25] inhibiting the light penetration inside by the large surface coverage of NS on ZIS.

Photocatalytic H_2 evolution using NS and NS/NIS has been performed in the presence of lactic acid as the sacrificial agent. As shown in Fig. 5c, H_2 evolution increased with increasing irradiation time and

Fig. 5. Photocatalytic H_2 evolution rate using pure ZIS and NS/ZIS-10 in the presence of methanol and lactic acid (a). H_2 evolution rate using NS/ZIS-x under the irradiation at 420 nm in the presence of lactic acid (b). Time profiles of H_2 evolution under the irradiation at 420 nm using pure ZIS and NS/ZIS-x (c). Recycled H_2 evolution under the irradiation at 420 nm using NS/ZIS-10 (d).

amount of NS loading, indicating that NS addition effectively increases H_2 evolution of ZIS without additive Pt co-catalyst. Additionally, the photocatalytic stability of NS/ZIS-10 for H_2 evolution was examined by repeating the experiment three times. After each time, the catalysts were isolated from the reaction solutions by centrifugation, washed with deionized water, and repeated above experiment. Apparently, the photocatalytic activity of NS/ZIS-10 remains essentially unchanged during three cycles (Fig. 5d). The crystal structure of NS/ZIS-10 shows no obvious change after 5 h, indicating the sufficient photostability of NS/ZIS-10. For the third repeated experiment, the photocatalytic activity still remains within 5% decrease.

To further understand the mechanism of efficient photocatalytic activity and photocurrent performance of NS/ZIS-x, the incident photon to current conversion efficiency was measured at 0 V bias under the light irradiation. Apparent quantum efficiency (AQE) is calculated from Eq. (2):

$$\text{AQE} (\%) = \frac{\text{Number of reacted electrons}}{\text{Number of incident photons}} \times 100 = \frac{2n_{\text{H}_2}}{n_p} \times 100 \quad (2)$$

where n_{H_2} and n_p are numbers of evolved H_2 molecules and incident photons, respectively [26,27]. As shown in Fig. 6, AQE significantly reduces with decreasing the light energy. The AQE difference between 32% at 420 nm and zero at 500 nm can not be interpreted by the difference of the absorption spectrum in which NS loading has no influence on the irradiation at 500 nm, although the absorption increases in the range of 599–750 nm. In other word, the efficient H_2 evolution results from the enhanced charge transfer and suppressed low recombination.

Above UV-vis and AQE results have confirmed the information on

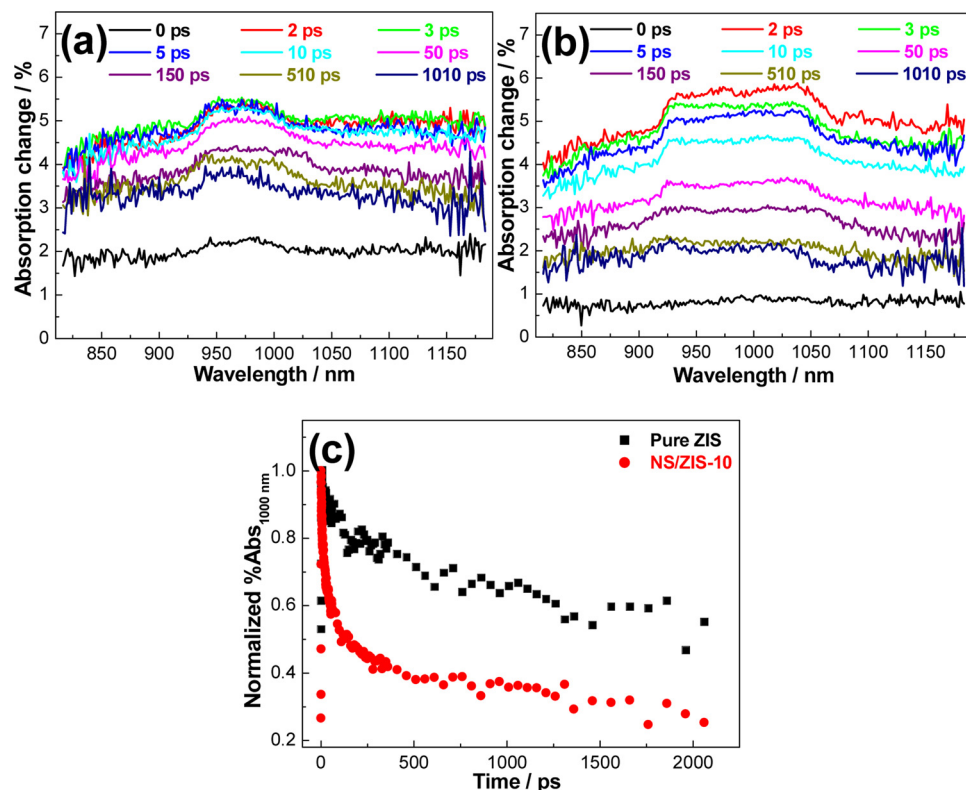


Fig. 7. Time-resolved diffuse reflectance spectra observed at various times after a laser flash for pure ZIS (a) and NS/ZIS-10 (b). Time profiles of normalized transient absorption at 1000 nm for pure ZIS and NS/ZIS-10 (c).

efficient charge transfer and low charge recombination in NS/ZIS-x. It is widely accepted that efficient charge transfer and low carrier recombination are crucial to the enhancement of photocatalytic performance. Therefore, it is very important to further make clear the detailed charge carrier dynamics, which would contribute to understanding the ultrafast process in photocatalytic reactions. Here time-resolved diffuse reflectance (TDR) spectroscopy was performed to analyze the initial charge lifetimes under visible light irradiation. As shown in Fig. 7a, a weak transient absorption signal was observed in the range of 920–1020 nm at various times after a laser flash, assigned to trapped and free (or shallowly trapped) electrons in pure ZIS. Similarly, a broad absorption band was also observed in the range of 910–1050 nm at various times after a laser flash for NS/ZIS-10 (Fig. 7b). In contrast, the absorption signals are slightly higher and wider than that of pure ZIS, indicating that electrons are generated more efficiently in NS/ZIS-10.

The time profiles of the transient absorption decays at 1000 nm for pure ZIS and NS/ZIS-10 were fitted by two-exponential functions (Fig. 7c and Table 2). Usually, two lifetimes of τ_1 and τ_2 for pure semiconductor and two-semiconductor heterostructures represent the charge recombination of electron-hole pairs with shorter and longer distances, respectively [28–30]. τ_1 for NS/ZIS-10 (13 ps) is 3.5-fold shorter than that for pure ZIS (45 ps), τ_2 for NS/ZIS-10 (252 ps) is five-fold shorter than that for pure ZIS (1240 ps), and the average lifetime (τ_{ave}) in NS/ZIS-10 (241 ps) is five-fold shorter than that in pure ZIS (1230 ps). The shorter lifetimes indicate that the photogenerated

electrons of ZIS are efficiently transferred to the conduction band (CB) of NS in NS/ZIS-10. Consequently, the charge recombination with longer distance is suppressed greatly in NS/ZIS. Further increasing Ni^{2+} solutions also causes shorter τ_{ave} , but more NS contents also impede the light absorption and light excitation (Figure S5).

Furthermore, photocurrent response and electrochemical impedance spectroscopy (EIS) were also measured to explore the photoelectrochemical potential, interface electron transfer, and charge recombination in electrodes using pure ZIS and NS/ZIS-x under the irradiation at 420 nm. As shown in Fig. 8a, ZIS and NS/ZIS-x electrodes show a sensitive and stable photocurrent response. Importantly and interestingly, NS/ZIS-x generates a more stable and higher photocurrent, showing that NS loading favors more intensive light harvesting, more efficient electron-hole separation, and faster charge transfer. However, photocurrent gradually decreases to 75% after 350 s. The effect of interfacial charge transfer and separation is further evidenced by EIS analysis (Fig. 8b). The equivalent circuit can be fitted the EIS spectra from the inset scheme [31–33], where R_s , R_{ct} , C_{ct} , and W_o represent the internal resistance, the charge transfer resistance, double-layer capacitance of the electrode–electrolyte interface, and Warburg resistance, respectively. In general, charge transfer property is determined by lower charge transfer resistance and smaller diameter of the semicircle arc in high frequency zone [34–36]. It can be clearly seen that the semicircle diameter in high frequency region for NS/ZIS electrode is slightly smaller than that of ZIS. Namely, the formation of NS/ZIS-x heterostructure decreases interfacial reaction resistance, accelerates interfacial electron transfer, and improves the charge recombination. Consequently, a more efficient separation of photogenerated electron–hole pairs can be generated in NS/ZIS-x. The phenomenon is attributed to the formation of the space electric field at NS/ZIS interfaces, which favors the charge separation with high efficiency. In a word, TDR, photocurrent, and EIS confirm that NS/ZIS-x possess efficient photocatalytic activity because of the enhanced charge separation and faster charge transfer.

Table 2

Lifetimes of the electrons from the transient absorption decays at 1000 nm.^a

Samples	τ_1 (ps)	τ_2 (ps)	τ_{ave} (ps)
Pure ZIS	45 (24%)	1240 (76%)	1230
NS/ZIS-10	13 (50%)	252 (50%)	241

^a Ratios of τ_1 and τ_2 components in the parentheses.

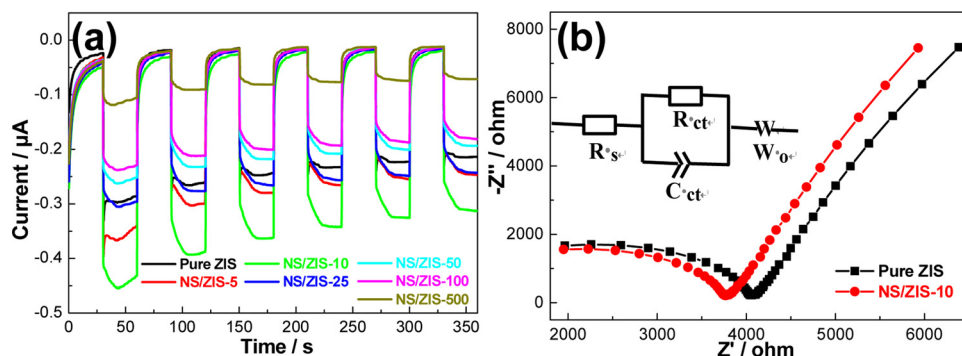


Fig. 8. Photocurrent responses of pure ZIS and NS/ZIS-x under the irradiation at 420 nm (a). Nyquist impedance plots of EIS for pure ZIS and NS/ZIS-10 (b).

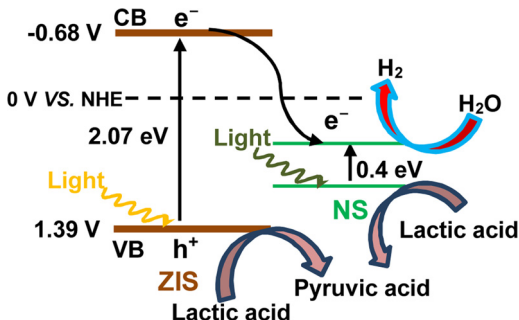


Fig. 9. Photocatalytic H₂ evolution using NS/ZIS in the presence of lactic acid.

Based on the experimental results, the photocatalytic H₂ evolution using NS/ZIS in the presence of lactic acid can be explained by the charge transfer processes at the interface and surfaces of NS and ZIS as shown in Fig. 9.

Firstly, valence band (VB) and CB potentials of pure ZIS and pure NS are determined according to Eqs. (3) and (4) [37]:

$$E_{VB} = X - E' + 0.5E_g \quad (3)$$

$$E_{CB} = E_{VB} - E_g \quad (4)$$

where E_{VB} and E_{CB} are the VB and CB potential energies, respectively, X is the geometric mean of the absolute electronegativity, E' is the energy of free electrons on the hydrogen scale (4.5 eV vs. NHE), and E_g is the band gap energy. For ZIS, X and E_g are 4.87 and 2.07 eV, respectively. Then, E_{VB} and E_{CB} of ZIS are calculated to be 1.39 and -0.68 eV, respectively. Similarly, E_{VB} and E_{CB} of NS are calculated to be 0.95 and 0.55 eV, respectively. When NS and ZIS were irradiated with the visible light, both are excited to generate electron-hole pairs. Due to the potential difference of CB and VB, the photogenerated electrons in CB of ZIS can readily transfer to CB of NS via hetero-junctioned interfaces. Above TDR results confirm that the electron transfer is very fast. At the same time, the photogenerated hole on the surface of ZIS can react with lactic acid to form pyruvic acid [38]. Consequently, the effectively spatial separation of photogenerated electron-hole pair for NS/ZIS-x is significantly enhanced. Higher electron charge concentration finally results in more efficient H₂ evolution. We also used XPS VB method to obtain VB and CB potential energies, and confirmed the same results (Supporting information Figure S6) [39]. The effects of NS and ZIS contribute to the formation of the unique charge transfer nanochannels in the heterojunction. These high-speed charge transfer and good heterojunction interfaces endowed by the heterojunction significantly shorten the charge migration distance and transfer time, ultimately leading to efficient photocatalytic activity for NS/ZIS-x.

3. Conclusions

We have elucidated the visible-light photocatalytic activity of ZIS

modified with NS. Due to NS loading, more than 300% enhancement of photocatalytic activities was observed in NS/ZIS-x, compared to pure ZIS. The relation between UV-vis absorption spectra and AQE shows that NS contributes to efficient light absorption but not photocatalytic activity. The photocurrent and EIS experiments show higher photocurrent and significantly decreasing photochemical impedance for NS/ZIS-x. Consequently, the efficient H₂ evolution results from enhanced interfacial electron transfers, retarded electron-hole recombination process, and enhanced charge separation. It should be noted that heterostructures are beneficial for applications in the field of photocatalysis.

Acknowledgements

We thank Mrs. Daming Ruan and Ke Zhang, SANKEN, Osaka University, for their assistance for the experiments. We are thankful for the help of the Comprehensive Analysis Center of SANKEN, Osaka University. This work has been partly supported by a Grant-in-Aid for Scientific Research (Project 25220806 and others) from the Ministry of Education, Culture, Sports, Science and Technology (MEXT) of the Japanese Government, and the Fundamental Research Funds for the Central Universities (2017XKQY010), China. A.Y. would like to acknowledge “Special foundation for Overseas Training Program of Excellent Young Teachers and Principals in Jiangsu Province”.

Appendix A. Supplementary data

Supplementary material related to this article can be found, in the online version, at doi:<https://doi.org/10.1016/j.apcatb.2019.02.075>.

References

- [1] X. Jiao, Z. Chen, X. Li, Y. Sun, S. Gao, W. Yan, C. Wang, Q. Zhang, Y. Lin, Y. Luo, Y. Xie, Defect-mediated electron-hole separation in one-unit-cell ZnIn₂S₄ layers for boosted solar-driven CO₂ reduction, *J. Am. Chem. Soc.* 139 (2017) 7586–7594.
- [2] X.Y. Liu, H. Chen, R. Wang, Y. Shang, Q. Zhang, W. Li, G. Zhang, J. Su, C.T. Dinh, F.P.G. de Arquer, J. Li, J. Jiang, Q. Mi, R. Si, X. Li, Y. Sun, Y.T. Long, H. Tian, E.H. Sargent, Z. Ning, 0D–2D quantum dot: Metal dichalcogenide nanocomposite photocatalyst achieves efficient hydrogen generation, *Adv. Mater.* 29 (2017) 1605646.
- [3] M. Liu, Y. Chen, J. Su, J. Shi, X. Wang, L. Guo, Photocatalytic hydrogen production using twinned nanocrystals and an unanchored NiS_x co-catalyst, *Nat. Energy* 1 (2016) 1–8.
- [4] W. Yang, L. Zhang, J. Xie, X. Zhang, Q. Liu, T. Yao, S. Wei, Q. Zhang, Y. Xie, Enhanced photoexcited carrier separation in oxygen-doped ZnIn₂S₄ nanosheets for hydrogen evolution, *Angew. Chem. Int. Ed.* 55 (2016) 6716–6720.
- [5] F. Shi, L. Chen, M. Chen, D. Jiang, Ag-C₃N₄/nanocarbon/ZnIn₂S₄ nanocomposite: An artificial Z-scheme visible-light photocatalytic system using nanocarbon as the electron mediator, *Chem. Commun.* 51 (2015) 17144–17147.
- [6] L. Ye, Z. Li, ZnIn₂S₄: a photocatalyst for the selective aerobic oxidation of amines to imines under visible light, *ChemCatChem* 6 (2014) 2540–2543.
- [7] L.L. Long, J.J. Chen, X. Zhang, A.Y. Zhang, Y.X. Huang, Q. Rong, H.Q. Yu, Layer-controlled growth of MoS₂ on self-assembled flower-like Bi₂S₃ for enhanced photocatalysis under visible light irradiation, *NPG Asia Mater.* 8 (2016) 263.
- [8] J.S. Ross, P. Rivera, J. Schaibley, E. Lee-Wong, H. Yu, T. Taniguchi, K. Watanabe, J. Yan, D. Mandrus, D. Cobden, W. Yao, X. Xu, Interlayer exciton optoelectronics in

- a 2D heterostructure *p–n* junction, *Nano Lett.* 17 (2017) 638–643.
- [9] D.S. Koda, F. Bechstedt, M. Marques, L.K. Teles, Coincidence lattices of 2D crystals: Heterostructure predictions and applications, *J. Phys. Chem. C* 120 (2016) 10895–10908.
- [10] D. Zeng, L. Xiao, W.J. Ong, P. Wu, H. Zheng, Y. Chen, D.L. Peng, Hierarchical $ZnIn_2S_4/MoSe_2$ nanoarchitectures for efficient noble-metal-free photocatalytic hydrogen evolution under visible light, *ChemSusChem* 10 (2017) 4624–4631.
- [11] S. Wang, B.Y. Guan, X.W.D. Lou, Construction of $ZnIn_2S_4$ – In_2O_3 hierarchical tubular heterostructures for efficient CO_2 photoreduction, *J. Am. Chem. Soc.* 140 (2018) 5037–5040.
- [12] S. Zhang, X. Liu, C. Liu, S. Luo, L. Wang, T. Cai, Y. Zeng, J. Yuan, W. Dong, Y. Pei, Y. Liu, MoS_2 quantum dot growth induced by S vacancies in a $ZnIn_2S_4$ monolayer: Atomic-level heterostructure for photocatalytic hydrogen production, *ACS Nano* 12 (2018) 751–758.
- [13] W. Li, Z. Lin, G. Yang, A 2D self-assembled $MoS_2/ZnIn_2S_4$ heterostructure for efficient photocatalytic hydrogen evolution, *Nanoscale* 9 (2017) 18290.
- [14] B. Xu, P. He, H. Liu, P. Wang, G. Zhou, X. Wang, A 1D/2D helical $CdS/ZnIn_2S_4$ nano-heterostructure, *Angew. Chem. Int. Ed.* 53 (2014) 2339–2343.
- [15] M.Q. Yang, Y.J. Xu, W. Lu, K. Zeng, H. Zhu, Q.H. Xu, G.W. Ho, Self-surface charge exfoliation and electrostatically coordinated 2D hetero-layered hybrids, *Nat. Commun.* 8 (2017) 14224.
- [16] S.J. Peng, L.L. Li, Y.Z. Wu, L. Jia, L.L. Tian, M. Srinivasan, S. Ramakrishna, Q.Y. Yan, S.G. Mhaisalkar, Size- and shape-controlled synthesis of $ZnIn_2S_4$ nanocrystals with high photocatalytic performance, *CrystEngComm* 15 (2013) 1922–1930.
- [17] Z. Chen, D. Li, W. Zhang, C. Chen, W. Li, M. Sun, Y. He, X. Fu, Low-temperature and template-free synthesis of $ZnIn_2S_4$ microsphere, *Inorg. Chem.* 47 (2008) 9766–9772.
- [18] H. Xu, Y. Jiang, X. Yang, F. Li, A. Li, Y. Liu, J. Zhang, Z. Zhou, L. Ni, Fabricating carbon quantum dots doped $ZnIn_2S_4$ nanoflower composites with broad spectrum and enhanced photocatalytic tetracycline hydrochloride degradation, *Mater. Res. Bull.* 97 (2018) 158–168.
- [19] G. Kalaiyaranan, K. Aswathi, J. Joseph, Formation of nanoporous NiS films from electrochemically modified GC surface with nickel hexacyanoferrate film and its performance for the hydrogen evolution reaction, *Int. J. Hydrogen Energy* 42 (2017) 22866–22876.
- [20] H. Zhao, H. Zhang, G. Cui, Y. Dong, G. Wang, P. Jiang, X. Wu, N. Zhao, A photochemical synthesis route to typical transition metal sulfides as highly efficient cocatalyst for hydrogen evolution: from the case of NiS/g-C₃N₄, *Appl. Catal. B-Environ.* 225 (2018) 284–290.
- [21] S.S. Abdullahi, S. Güner, Y. Koseoglu, I.M. Musa, B.I. Adamu, M.I. Abdulhamid, Simple method for the determination of band gap of a nanopowdered sample using Kubelka Munk theory, *J. Niger. Assoc. Math. Phys.* 35 (2016) 241–246.
- [22] Y. Yu, G. Chen, G. Wang, Z. Lv, Visible-light-driven $ZnIn_2S_4/CdIn_2S_4$ composite photocatalyst with enhanced performance for photocatalytic H_2 evolution, *Int. J. Hydrogen Energy* 38 (2013) 1278–1285.
- [23] C.H.M. Chung, P.R. Brown, V. Bulović, M.G. Bawendi, Improved performance and stability in quantum dot solar cells through band alignment engineering, *Nat. Mater.* 13 (2014) 796–801.
- [24] L. Bai, X. Cai, J. Lu, L. Li, S. Zhong, L. Wu, P. Gong, J. Chen, S. Bai, Surface and interface engineering in $Ag_2S@MoS_2$ core–shell nanowire heterojunctions for enhanced visible photocatalytic hydrogen production, *ChemCatChem* 10 (2018) 2107–2114.
- [25] I. Vamvasakis, B. Liu, G.S. Armatas, Size effects of platinum nanoparticles in the photocatalytic hydrogen production over 3D mesoporous networks of CdS and Pt nanojunctions, *Adv. Funct. Mater.* 26 (2016) 8062–8071.
- [26] Y. Yan, R.W. Crisp, J. Gu, B.D. Chernomordik, G.F. Pach, A.R. Marshall, J.A. Turner, M.C. Beard, Multiple exciton generation for photoelectrochemical hydrogen evolution reactions with quantum yields exceeding 100%, *Nat. Energy* 2 (2017) 17052.
- [27] Z. Zheng, T. Tachikawa, T. Majima, Single-particle study of Pt-modified Au nanorods for plasmon-enhanced hydrogen generation in visible to near-infrared region, *J. Am. Chem. Soc.* 136 (2014) 6870–6873.
- [28] A. Furube, T. Asahi, H. Masuhara, H. Yamashita, M. Anpo, Charge carrier dynamics of standard TiO_2 catalysts revealed by femtosecond diffuse reflectance spectroscopy, *J. Chem. Phys. B* 103 (1999) 3120–3127.
- [29] P. Zhang, T. Tachikawa, M. Fujitsuka, T. Majima, Efficient charge separation on 3D architectures of TiO_2 mesocrystals packed with a chemically exfoliated MoS_2 shell in synergistic hydrogen evolution, *Chem. Commun.* 51 (2015) 7187–7190.
- [30] I. Grigioni, K.G. Stamplecoskie, E. Sell, P.V. Kamat, Dynamics of photogenerated charge carriers in $WO_3/BiVO_4$ heterojunction photoanodes, *J. Chem. Phys. C* 119 (2015) 20792–20800.
- [31] M.Y. Ye, Z.H. Zhao, Z.F. Hu, L.Q. Liu, H.M. Ji, Z.R. Shen, T.Y. Ma, 0D/2D heterojunctions of vanadate quantum dots/graphitic carbon nitride nanosheets for enhanced visible-light-driven photocatalysis, *Angew. Chem. Int. Ed.* 56 (2017) 8407–8411.
- [32] Y. Hou, Z. Wen, S. Cui, X. Guo, J. Chen, Constructing 2D porous graphitic C₃N₄ nanosheets/nitrogen-doped graphene/layered MoS_2 ternary nanojunction with enhanced photoelectrochemical activity, *Adv. Mater.* 25 (2013) 6291–6297.
- [33] Y. Choi, N. Yoon, N. Kim, C. Oh, H. Park, J.K. Lee, Discrete hollow carbon spheres derived from pyrolytic copolymer microspheres for Li-S batteries, *J. Electrochem. Soc.* 166 (2019) 5099–5108.
- [34] J. Tian, P. Hao, N. Wei, H.Z. Cui, H. Liu, 3D Bi_2MoO_6 nanosheet/ TiO_2 nanobel heterostructure: enhanced photocatalytic activities and photoelectrochemistry performance, *ACS Catal.* 5 (2015) 4530–4536.
- [35] Q. Liu, H. Lu, Z. Shi, F. Wu, J. Guo, K. Deng, L. Li, 2D $ZnIn_2S_4$ nanosheet/1D TiO_2 nanorod heterostructure arrays for improved photoelectrochemical water splitting, *ACS Appl. Mater. Inter.* 6 (2014) 17200–17207.
- [36] I. Ledezma-Yanez, W.D.Z. Wallace, P. Sebastián-Pascual, V. Climent, J.M. Feliu, M.T.M. Koper, Interfacial water reorganization as a pH-dependent descriptor of the hydrogen evolution rate on platinum electrodes, *Nat. Energy* 2 (2017) 17031.
- [37] J. Hou, C. Yang, H. Cheng, Z. Wang, S. Jiao, H. Zhu, Ternary 3D architectures of CdS QDs/graphene/ $ZnIn_2S_4$ heterostructures for efficient photocatalytic H_2 production, *Phys. Chem. Chem. Phys.* 15 (2013) 15660–15668.
- [38] Y. Zhang, Z. Peng, S. Guan, X. Fu, Novel β -NiS film modified CdS nanoflowers heterostructure nanocomposite: extraordinarily highly efficient photocatalysts for hydrogen evolution, *Appl. Catal. B-Environ.* 224 (2018) 1000–1008.
- [39] G. Liu, P. Niu, L. Yin, H. Cheng, α -Sulfur crystals as a visible-light-active photocatalyst, *J. Am. Chem. Soc.* 134 (2012) 9070–9073.